

ORIGINAL RESEARCH PAPER

## Synthesis of Zinc aluminate nanoparticles from aluminum / zinc sludge for degradation of brilliant cresyl blue under visible light irradiation

Asmaa A. Abd-Allah<sup>1</sup>, Yasser M. Z. Ahmed<sup>2\*</sup>, Said M. El-Sheikh<sup>3\*</sup>, Ahmed O. Youssef<sup>f</sup>, Amira M. M. Amin<sup>2\*</sup>

<sup>1</sup> Chemistry Department, Faculty of Science, Ain Shams University, Abbassia, Cairo, Egypt.

<sup>2</sup> Refractory and Ceramic Materials Department, Central Metallurgical Research and Development Institute, CMRDI, Helwan 11421, Egypt.

<sup>3</sup> Nanostructure Materials Department, Central Metallurgical Research and Development Institute, CMRDI, Helwan 11421, Egypt.

Received: 2022-05-21

Accepted: 2022-06-27

Published: 2022-07-01

### ABSTRACT

Scientists and researchers from all over the world are paying close attention to the recycling of industrial waste into new materials. Aluminum and zinc sludge powders were gathered from aluminum sheets and big iron manufacturers to be used as starting materials in the synthesis of zinc aluminate nanoparticles. The XRF, XRD, and DTA examinations were used to characterize the collected sludge powders. The main components of aluminum and zinc sludges, according to the findings, are gibbsite ( $\text{Al}(\text{OH})_3$ ) and hydrozincite ( $\text{Zn}_5(\text{CO}_3)_2(\text{OH})_6$ ), respectively. Without any primary advanced chemical treatments, the collected sludges were used to perform solid-state reaction (SSR) and molten salt synthesis (MSS) at  $1100^\circ\text{C}$ . XRD, FTIR, XPS, SEM, and TEM examinations were used to characterize the synthesized samples. Both SSR and MSS deduced pure phase zinc aluminate nanoparticles, with crystallite sizes of 17.4 and 12.7 nm for SSR and MSS samples, respectively. The microstructure of the MSS sample was characterized by a high structure homogeneity, whereas, the high degree of particle aggregation was shown by the SSR sample's microstructure. The optical properties of the synthesized SSR and MSS samples were studied by using UV-visible and PL spectroscopy. The bandgap energies for SSR and MSS samples were calculated to be 2.78 and 2.48 eV, respectively. These samples are utilized in the photocatalytic degradation of the brilliant cresyl blue dye (BCBD), owing to their tiny bandgap energies and high absorption efficiency. The photocatalytic degradation percent of BCBD reached 94.5% and 86.7% by using MSS and SSR samples, respectively, at the optimum conditions of pH (10), dye concentration (40 mg/l), and sample dose (1 g/l).

**Keywords:** solid state reaction, molten salt synthesis, industrial waste, zinc aluminate nanoparticles

### How to cite this article

Abd-Allah A.A, Ahmed Y.M.Z., El-Sheikh S.M., Youssef A.O., Amin A.M.M. Synthesis of Zinc aluminate nanoparticles from aluminum / zinc sludge for degradation of brilliant cresyl blue under visible light irradiation . J. Water Environ. Nanotechnol., 2022; 7(3): 288-305.

DOI: 10.22090/jwent.2022.03.005

### INTRODUCTION

Recently, researchers have made a concerted effort to direct their studies to the use of industrial wastes rather than commercial raw materials in the development of novel materials. The recovery of new materials from industrial wastes increases

the value of the new materials and appears to be an environmentally friendly and cost-effective route. Specifically, the supposed experimental techniques must avoid being high-cost and time-consuming. This is in order to exclude the disadvantages of literature research, which are represented by pricey materials and specialized apparatus.

Spinel-type mixed metal oxides, such as

\* Corresponding Author Email: [selsheikh2001@gmail.com](mailto:selsheikh2001@gmail.com), [amoustafa\\_eng@hotmail.com](mailto:amoustafa_eng@hotmail.com), [ahmedymz@hotmail.com](mailto:ahmedymz@hotmail.com)

zinc aluminate, are an important family of ceramic materials. Gahnite is a mineral that was discovered in nature with the spinel structure of zinc aluminate ( $ZnAl_2O_4$ ). It's an example of a compound with the generic formula  $(A)[B]O$ , with A and B being divalent and trivalent cations, respectively [1,2]. Zinc aluminate possesses high mechanical resistance, high chemical and thermal stability, and low surface acidity [3,4]. These outstanding qualities make these materials appropriate for a wide range of applications, including refractory materials, optical coatings for aerospace applications, and host matrices. Because of its wide bandgap energy, zinc aluminate is useful for UV photoelectronic applications (3-3.9 eV).<sup>[5]</sup> Zinc aluminate has recently been widely used as a photocatalyst in a variety of activities, including waste water treatment and photocatalytic degradation of organic pigments [6,7]. Zinc aluminate can also be employed as catalyst support in a variety of chemical transformations, including saturated alcohols' dehydration to olefins, paraffin dehydrogenation, methanol, and heavy alcohols' synthesis [2,8].

Because zinc aluminate is so important, numerous techniques have been utilized to synthesize it, including sol-gel, co-precipitation, hydrothermal, combustion, and solid-state reaction (SSR) [5,9-12]. The disadvantages of solid-state reactions are inhomogeneity, lack of stoichiometry control, high temperature, and reduced surface area [13]. However, the solid-state reaction has several advantages: it is straightforward to carry out, and the starting materials are frequently inexpensive. Solid reactions don't involve the use of solvents; hence, products don't require substantial purification to remove remnants of solvents and contaminants. The primary advantage of the solid-state reaction is the high yield of products, which can range from a few grams to several kilograms, making it more cost-effective than other synthesis processes [10].

The goal of current materials research is to overcome the drawbacks of solid-state reaction (SSR), such as the difficulties of producing nanosize and structural homogeneity. Molten salt synthesis (MSS) could be used for SSR modification [14], in which a salt with a low melting point could be utilized as a dissolving medium for preparing materials from their solid oxides and carbonates. As a molten salt, salts such as KCl, NaCl, LiCl, or a combination of two salts could be employed. In essence, reactants can be combined with molten

salt and heated to a temperature above their melting point. The ability of molten salt to dissolve all of the reactant particles and to operate as a suitable medium for the high mobility of liquid reactant particles is required for the synthesis of homogeneous nanosized particles. By increasing the contact area between the reactant particles, the synthesized particles spontaneously precipitate from the liquid phase and the rate of the solid-state reaction is increased. Nanoscale particles are easily created as the produced particles precipitate under the supersaturation of dissolved reactant particles. The desirable advantage of molten salt synthesis is that it doesn't react with the reactants or the products and can be easily removed by washing with distilled water. As a result, the value of molten salt can be concluded in terms of improving reaction rates and reaching the nanoscale with a homogeneous structure [15].

In this study, zinc aluminate nanoparticles were synthesized from industrial waste using solid-state reaction and molten salt synthesis. Which, the overall goals were summarized as the following: recycling of solid industrial waste, which represents a significant burden to dispose of and transport. Investigating the ability of SSR and MSS to synthesize zinc aluminate nanoparticles. Performing structural, morphological, and optical characterizations for the synthesized samples. Utilizing the SSR and MSS samples in the photocatalytic degradation of the harmful and complex structure of brilliant cresyl blue dye.

## METHODOLOGY

### *Sludge collection:*

Industrial wastes are represented in the aluminum and zinc sludge powders; aluminum sludge is formed during the fabrication of aluminum sheets in ALUIMISR (aluminum manufacturing company-Egypt). In addition, zinc sludge is generated during blast furnace operations for large-scale iron production in Egypt's Iron and Steel Company. The blast furnace sludge produced during the extraction of iron from its ore and conversion into alloys contains a variety of contaminants in addition to Fe and C. Zn is the most problematic of these impurities because it evaporates at a lower temperature at the start of the metallurgical process and subsequently condenses on the blast furnace walls. The condensed Zn produces a lot of dust, which might harm the furnace coating. It also prevents the furnace load

(a mix of iron ores, additives, and cokes) from dropping, resulting in a sudden drop in the load. The evaporated Zn is evacuated from the blast furnace in three ways: some of it escapes through the gas flow and condenses on dust particles, which are then removed by the air pollution control system. Sludge is created when the smaller particles are cleaned out with a wet scrubber. Large particles (>50  $\mu$ m) are cleaned with flue gas in a dust bag and a cyclone, and can then be sintered directly in the blast furnace [16]. XRF, XRD, and DTA analyses were used to evaluate the collected zinc and aluminum sludge.

#### *Zinc aluminate synthesis by SSR and MSS*

Aluminum and zinc sludge powders were combined in a solid-state reaction at a 2: 1 molar ratio of Al: Zn, estimated using the XRF weight percent of Zn and Al compounds in their sludges. A ball milling device is used to accurately grind the sludges mixture for 1 h at 300 rpm in the presence of distilled water. The ground powder was removed from the miller's container and placed on a petri dish, where it was dried overnight at 100°C. The dried mixed powder was ground in an agate mortar, compacted into 5 gm pellets, and calcined in a muffle furnace at 1100°C for 5 h at 3°C/min. The heated pellets were removed from the furnace and re-ground in an agate mortar before being rinsed with warm distilled water and dried at 100°C for 1 h before being characterized.

For employing the molten salt synthesis, potassium chloride (KCl) was added to the sludges' mixture in a 4: 1 potassium chloride: zinc aluminate weight ratio and the mixture was manually ground extremely well.

#### *Photocatalytic degradation of brilliant cresyl blue dye (BCBD)*

Under visible light irradiation, photocatalytic degradation of the bright cresyl blue dye (molecular weight = 385.96 g mol<sup>-1</sup>) was accomplished using a halogen lamp (FSE-1000 W, 220/240 V, 50/60 HZ, made in China). The dye stock solution was prepared at a concentration of 40 mg/l and about 0.2 gm of SSR and MSS sample powder was separately added to 200 ml of the dye solution. For assessing the produced materials' activity in the adsorption of BCBD, the dye/sample solution was stirred in the dark for 1 h. Beyond the dark test, the sample solution was exposed to visible light for an additional 3 h while being constantly

stirred. During the light exposure, about 2 ml of the sample batch was taken in a test tube at constant time intervals for absorbance measurements using UV-visible absorption spectra. The pH effect was studied by varying the pH of the dye solution from 5-10. The sample dose effect was investigated by varying the MSS sample dose from 0.25 to 1 g/l at a constant pH of 10 and a dye concentration of 40 mg/l, as taken from an earlier pH investigation. Using 1 g/l of MSS sample at optimal pH 10, the dye concentration effect was investigated by varying the dye concentration from 40 to 80 mg/l. The recyclable test was used to assess the photocatalytic stability of the MSS sample over numerous runs under optimal pH, sample dose, and dye concentration conditions. The used powder was filtered and activated for the next run by washing it with distilled water and ethanol, then drying it. To corroborate the results obtained at optimum conditions using the MSS sample, total organic carbon (TOC) analysis was employed.

#### *Materials characterization*

To characterize the collected industrial waste and synthesized zinc aluminate samples, X-ray diffraction (XRD, Bruker axis D8, Germany) with Cu-K $\alpha$  ( $\lambda=1.5406$ ) radiation and a secondary monochromator in the range of 2 $\theta$ -scale from 4–70° was used. From X-ray diffraction data using the Debye–Scherrer formula ( $d_{RX} = K\lambda/\beta \cos \theta$ ), the crystallite size of the synthesized SSR and MSS samples was estimated. Where  $d_{RX}$  is the crystallite size,  $K=0.9$  is a correction factor to account for particle shapes,  $\lambda$  is the wavelength of Cu target = 1.5406 Å,  $\beta$  is the full width at half maximum (FWHM) of the most intense diffraction peak and  $\theta$  is the Bragg angle. An X-ray fluorescence (XRF) analyzer, model advanced Axios Netherlands, was used to determine the chemical composition of aluminum and zinc sludges. Differential thermal analysis (DTA) was performed on the collected sludges using a NETZSCH STA 409 C/CD equipment in the air at a rate of 10°C/min from ambient temperature to 1100°C. This is in terms of thermal gravimetric analysis (TG) and differential scanning calorimetry (DSC). FTIR spectra obtained in the range of 400-4000 cm<sup>-1</sup> were used to determine reaction completion using a JASCO FT/IR-6300 type A. Within an energy range of up to 4 KeV, the elemental composition of the synthesized samples was determined using Thermo Scientific™ K-Alpha™ X-ray photoelectron spectroscopy

(XPS), Al-K Micro-focused monochromator. The microstructure of zinc aluminate samples was studied using a JEOL scanning electron microscope (SEM) model JSM-5410 with a 20 KV accelerating voltage. High-resolution transmission electron microscopy with an acceleration voltage up to 120 kV, a magnification power up to 600 k, and a resolving power down to 0.2 nm (TEM, JEOL-JEM-1230, Tokyo, Japan) were used to analyze the morphology of samples, including particle size and shape. The histograms were constructed with the aid of the Image J software, Wayne Rasband, National Institute of Health, USA. The resulting zinc aluminate samples' optical properties were investigated by UV-visible absorption spectra and PL emission spectra for bandgap measurements. The absorption spectra are recorded at room temperature using a JASCO Corp. V-570, Rev. 1.00 spectrometer/data system at 200 to 1000 nm. At room temperature, a spectrofluorometer (RF-5301 equipment utilized by spectral Type EM) was used to measure photoluminescence (PL) emission spectra, with a 320 nm excitation wavelength and a scan range of 220-900 nm.

## RESULT AND DISCUSSION

### Collected industrial wastes

For aluminum and zinc sludges, XRF analysis

was used to determine the chemical composition and weight percent of all compounds found in the sludges. After ignition at 1000°C, XRF analysis of Al and Zn sludge samples shows weight losses of 39.2% and 26.6%, respectively. The weight percent of all the included compounds is listed in Table 1.

Figs. 1A and B show the XRD patterns of aluminum and zinc sludges, respectively. Fig. 1A depicts peaks that appeared at  $2\theta = 18.24^\circ, 20.24^\circ, 32.31^\circ, 33.78^\circ, 36.51^\circ, 36.51^\circ, 37.59^\circ, 39.30^\circ, 40^\circ, 41.59^\circ, 44.14^\circ, 45.35^\circ, 46.10^\circ, 47.29^\circ, 50.54^\circ, 52.17^\circ, 54.28^\circ, 63.73^\circ, 64.53^\circ, 66.11^\circ, \text{ and } 68.81^\circ$ , which are in agreement with the gibbsite mineral ( $\text{Al}(\text{OH})_3$ ) standard card (JCPDS, 70-2038) [17]. Fig. 1B displays peaks at  $2\theta = 13.06^\circ, 24.07^\circ, 25.03^\circ, 28.24^\circ, 31.09^\circ, 32.88^\circ, 33.46^\circ, 35.99^\circ, 38.84^\circ, 43.10^\circ, 47.16^\circ, 53.65^\circ, 58.13^\circ, \text{ and } 60.00^\circ$ , which correspond to the hydrozincite ( $\text{Zn}_5(\text{CO}_3)_2(\text{OH})_6$ ) phase standard card (JCPDS, 72-1100) [18]. The XRD spectra of aluminum and zinc sludges don't reveal any peaks related to the other phases, which were detected by minor traces in XRF analysis. This means that the primary phases in their sludges are gibbsite and hydrozincite.

Thermal properties of the mixture containing gibbsite mineral ( $\text{Al}(\text{OH})_3$ ) and hydrozincite ( $\text{Zn}_5(\text{CO}_3)_2(\text{OH})_6$ ) by 2: 1 of Al: Zn were investigated by the differential thermal analysis (DTA).

Table 1. displays the weight percent of all components present in Zn and Al sludges after heating the sludge powders at 1000°C.

Compound formula	Zn-sludge (weight %)	Al-sludge (weight %)
Na <sub>2</sub> O	---	9.928
MgO	0.132	0.525
Al <sub>2</sub> O <sub>3</sub>	1.002	48.043
SiO <sub>2</sub>	0.976	0.393
P <sub>2</sub> O <sub>5</sub>	0.051	0.023
SO <sub>3</sub>	1.715	0.168
K <sub>2</sub> O	0.035	0.021
CaO	2.097	1.087
TiO <sub>2</sub>	0.2	0.03
Cr <sub>2</sub> O <sub>3</sub>	0.008	0.007
MnO	0.273	0.024
Fe <sub>2</sub> O <sub>3</sub>	3.219	0.450
NiO	---	0.005
CuO	0.017	0.026
ZnO	62.377	0.02
Ga <sub>2</sub> O <sub>3</sub>	---	0.004
As <sub>2</sub> O <sub>3</sub>	0.033	---
SrO	0.012	0.017
BaO	0.672	---
PbO	0.334	---
SnO <sub>2</sub>	---	0.013
F	0.188	---
Cl	0.062	---

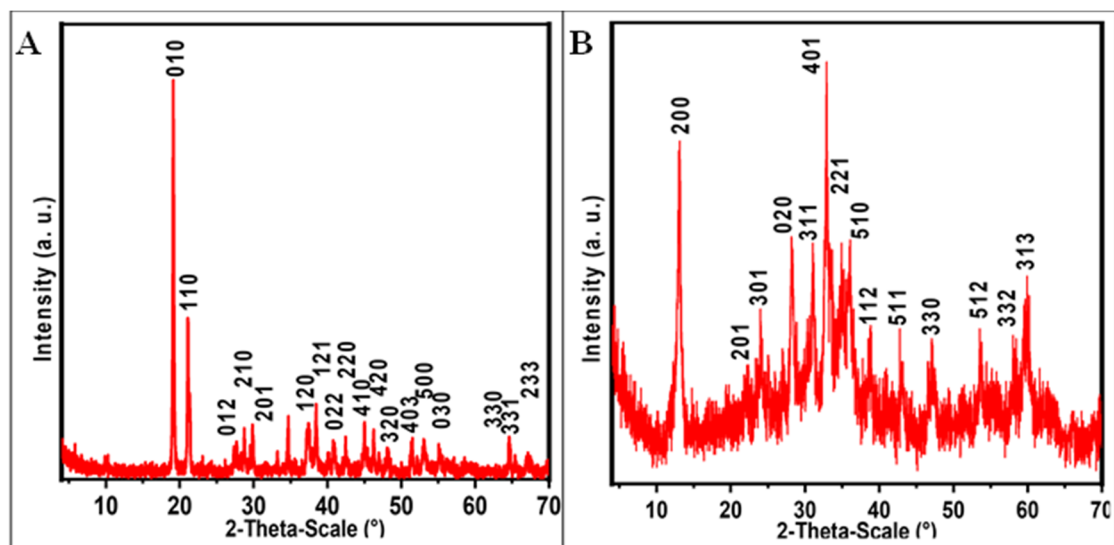


Fig. 1. XRD patterns of aluminum [A] and zinc [B] sludges.

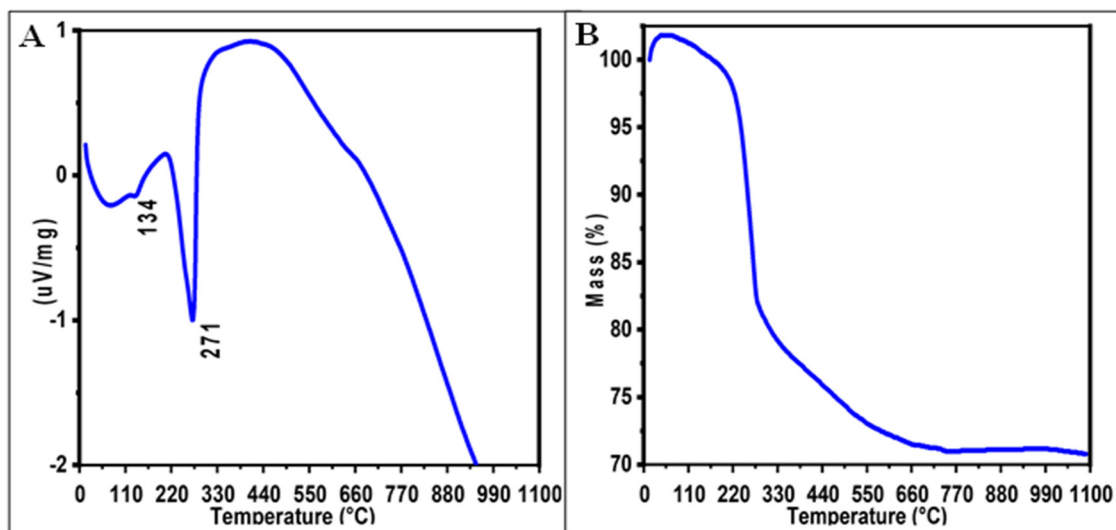
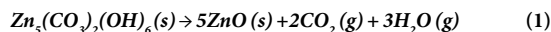


Fig. 2. differential thermal analysis in terms of DSC [A] and TG [B] of sludges' mixture.

Thermal analysis in terms of differential scanning calorimetry (DSC) and thermal gravimetry (TG) curves is shown in Figs. 2A and B, respectively. The DSC curve has two endothermic peaks (small and sharp) that are maximized at 134 & 271°C. The evaporation of surface adsorbed water molecules is responsible for the first peak (a minor endothermic peak). The fast-thermal decomposition of hydrozincite is responsible for the second peak (a sharp endothermic peak). This is consistent with the literature, which found the decomposition temperature of hydrozincite to be between 240 and 278°C [19–21], based on the reaction:



At the same time, it was discovered that gibbsite dehydroxylation occurs at roughly 270°C [22,23]. However, there are two options for the gibbsite transformation process that have been previously studied. The first option is the direct transformation to aluminum oxide ( $\text{Al}_2\text{O}_3$ ) (dehydroxylation), as described in reaction 2. The second is an indirect process that occurs when boehmite ( $\text{AlO}(\text{OH})$ ) is formed, which then changes to aluminum oxide, as shown in reactions 3 and 4.



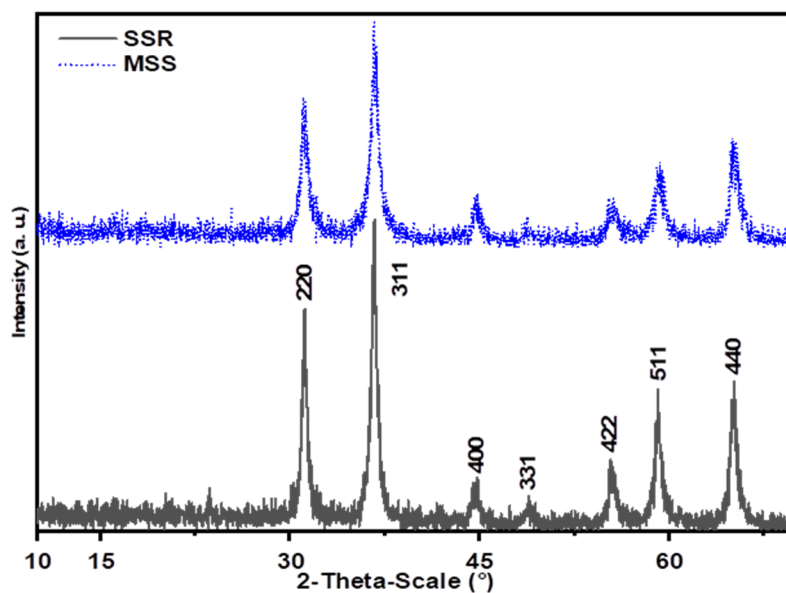
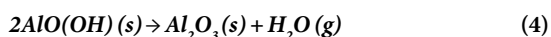


Fig. 3. XRD patterns of zinc aluminate samples synthesized by both SSR and MSS.



According to reaction 3, boehmite hydroxylation takes place around 500°C, as discussed in the literature. There is no endothermic peak on the DSC curve (Fig.2 A) near this temperature. As a result, gibbsite is converted directly to aluminum oxide via reaction 2 without passing through the intermediate production of boehmite.

The loss of water and carbon dioxide molecules from  $\text{Zn}_5(\text{CO}_3)_2(\text{OH})_6$  and  $2\text{Al}(\text{OH})_3$  heat decomposition resulted in a 28% weight loss, theoretically. According to reaction 1,  $\text{Zn}_5(\text{CO}_3)_2(\text{OH})_6$  (MW= 547 g/mol) loses ~ 25.95% of its weight during decomposition, in the form of two carbon dioxide molecules (88 g) and three water molecules (54 g) [20,21]. In addition, according to reaction 2 [22], two molecules of  $\text{Al}(\text{OH})_3$  (MW= 78 g/mol) lose ~ 34.5% in the form of three water molecules (54 g). The overall weight loss from the total mixture weight ( $547+78*2=703$ ) is represented by two carbon dioxide and six water molecules ( $88+54*2=196$  g). The TG curve shows a total weight loss of 30% for the sludge mixture, and it was predicted that the surface adsorbed water molecules would represent ~ 2% up to 134°C. The overall weight

loss was calculated using the TG curve, which corresponded to the theoretical weight loss based on thermal decomposition. The thermal decomposition of hydrozincite and gibbsite by reactions 1 and 2 is confirmed by TG analysis. Whereas, the extension of the weight loss in the TG curve to 730°C confirms that, the thermal decomposition of gibbsite and hydrozincite mixture didn't complete at a temperature lower than this. Finally, it was discovered that there is no extra weight loss above 730°C, implying that the sludges' mixture has thermal stability above 730°C due to the new phase formation.

#### Synthesized zinc aluminate samples

XRD analysis was used to determine the formation, purity, crystallinity, and crystallite size of samples synthesized using SSR and MSS, as shown in Fig. 3. The peaks of the two spectra appeared at  $2\theta = 31.26^\circ, 36.79^\circ, 44.87^\circ, 49.08^\circ, 55.63^\circ, 59.28^\circ, \text{ and } 65.25^\circ$ , respectively, for zinc aluminate (gahnite) (220), (311), (400), (331), (442), (511), and (440) crystal planes distance (JCPDS, 74-1136) [24]. SSR and MSS produced pure phase zinc aluminate, according to the XRD analysis. The SSR sample spectrum has higher peak intensities than the MSS sample spectrum, indicating that the SSR sample has a higher crystallinity. The Debye-Scherrer equation was used to calculate the average crystallite size, which was found to be 17.4 and

12.7 nm for samples synthesized by SSR and MSS, respectively. The nanosize of the produced samples is confirmed by the widening of peaks in XRD spectra.

X-ray photoelectron spectroscopy (XPS) was used to investigate the elemental composition of zinc aluminate samples synthesized by SSR and MSS, as shown in Fig. 4. The presence of elements such as Zn, Al, and O was detected in full surveys of SSR and MSS samples (Figs. 4A), with peaks appearing at 1044.44, 1021.42, 119.08, 978.09, 532.18, 531.22, and 73.56 eV. The two intense peaks at 1044.44 and 1021.42 eV correspond to zinc aluminate's Zn 2p energy levels (illustrated in the high-resolution Fig. 4B). The single peak at 978.09 eV corresponds to the carbonate species adsorbed on the surface as a result of the XPS instrument's calibration. The two peaks, which appeared at 119.08 and 73.56 eV correspond to the Al 2s and Al 2p energy levels, respectively (seen in high-resolution Fig. 4C). The crystalline and adsorbed O 1s energy levels are represented by two peaks, which appear at 532.18 and 531.22 eV, respectively (illustrated in the high-resolution Fig. 4D) [25]. The XPS investigation confirmed the reaction's completion and the formation of the  $ZnAl_2O_4$  structure, which was confirmed by the XRD analysis.

The formation and purity of zinc aluminate were investigated using FTIR spectra for samples synthesized by SSR and MSS, as illustrated in Fig. 5. The SSR and MSS spectra peaks are 496, 553, 661, 989, 1429, 1646, and 3415  $cm^{-1}$ . The sharp peak that appeared at 496  $cm^{-1}$  is a distinctive peak of zinc aluminate, and it corresponds to the stretching and bending vibration modes of Zn-O-Al, Al-O, and Zn-O [10,24]. Where, the peaks that appeared at 553 and 661  $cm^{-1}$  are corresponding to Al-O stretching and O-Al-O bending vibrations of the  $AlO_6$  group in the spinel type  $ZnAl_2O_4$  structure, respectively [24,26]. The minor two peaks that appeared at 989 and 1429  $cm^{-1}$  are corresponding to Al-OH bond bending mode [24], and they are more intense for the MSS sample. In addition, the two peaks that appeared at 1646 and 3415  $cm^{-1}$  are corresponding to O-H bending and stretching vibration modes of adsorbed surface water, respectively [24,26]. For samples synthesized by SSR or MSS, FTIR spectra revealed no impurity peaks, confirming the XRD and XPS findings of reaction completion at 1100°C and the creation of a single-phase zinc aluminate structure.

Scanning electron microscopy (SEM) was used to examine the structural morphology of zinc aluminate samples synthesized using SSR and MSS, as illustrated in Figs. 6A and B, respectively. In the microstructure of the SSR sample, there are plate-like particles with particle sizes ranging from 10 nm to 1  $\mu m$ , besides some huge patchy rods. In contrast to the SSR sample, structure homogeneity was visible in the microstructure of the MSS sample. In both routes, the variation in inhomogeneity is due to the reaction process and how the reactants are linked to one another. In solid-state reactions, there are two possible mechanisms. The first involves aluminum oxide as a spinel surface and zinc oxide as a diffusion ion. Zinc oxide ions penetrate the surface of aluminum oxide via vaporization, condensation, and surface diffusion. The zinc aluminate layer was formed after zinc oxide ions covered the aluminum oxide surface. Whereas, the second mechanism is more prospective in solid-state reactions because zinc and aluminum ions mutually diffuse through a sublattice of oxygen ions and then bond together [27].

In the case of molten salt synthesis, a large amount of potassium chloride salt was used as a solvent to completely dissolve the reactants. The MSS reaction mechanism was accomplished in two stages, the first being the reaction stage, which occurs in the first few minutes following the supersaturation of the solid solution by the dissolved reactant particles. By increasing the contact area between the reactant particles and achieving high mobility, molten salt addition increases the rate of the reaction [15,28]. As a result, the diffusion of zinc oxide to the aluminum oxide lattice in molten salt media must be much faster than in the SSR, allowing the reaction to proceed according to the first mechanism. At this stage, large plate-like particles with some surface roughness were produced, which was visible in image B.

After consuming all of the reactants' particles in the reaction stage, the second stage commenced, and it is known as the growth stage, in which the product particles are the only solid phase in the molten salt. The growth stage was primarily influenced by the phenomenon known as Ostwald ripening, which appeared with prolonged heating [28,29]. In which a large number of small product particles, which are still dissolved in the molten salt, participate on the surface of large particles, fall into the pores, and penetrate their kink. This phenomenon causes large particles to grow in size

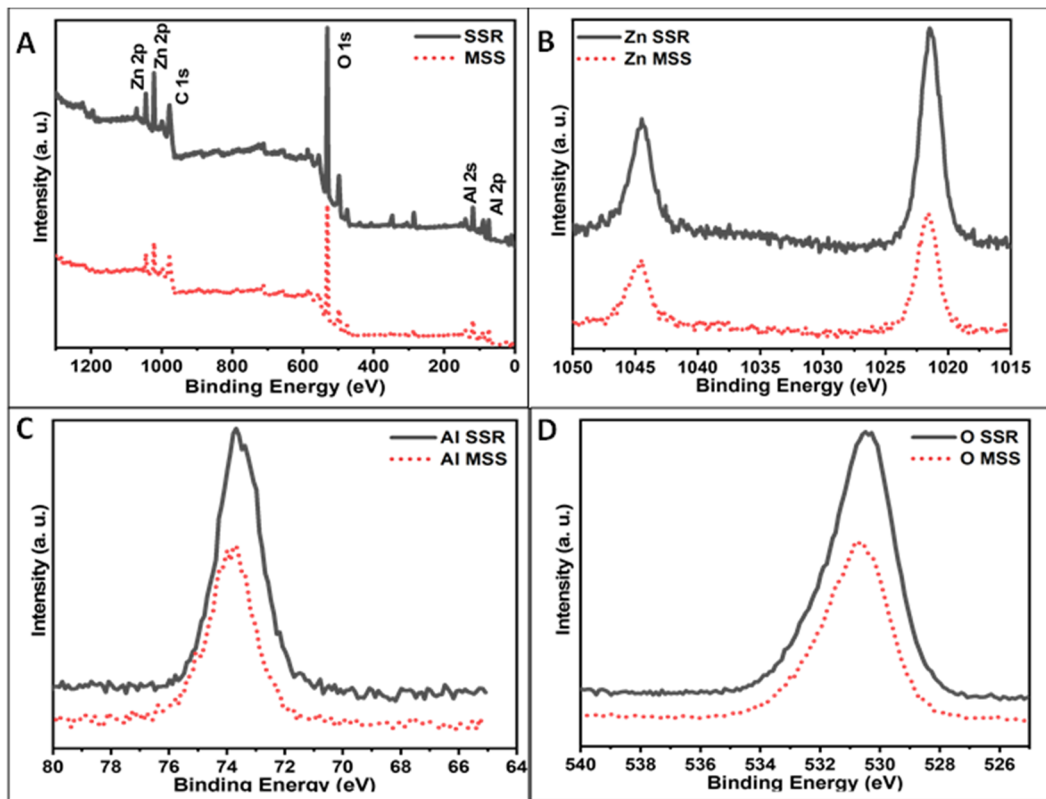


Fig. 4. XPS of zinc aluminate sample synthesized by both SSR and MSS, [A]: full survey, [B]: Zn 2p, [C]: Al 2p and [D]: O 1s.

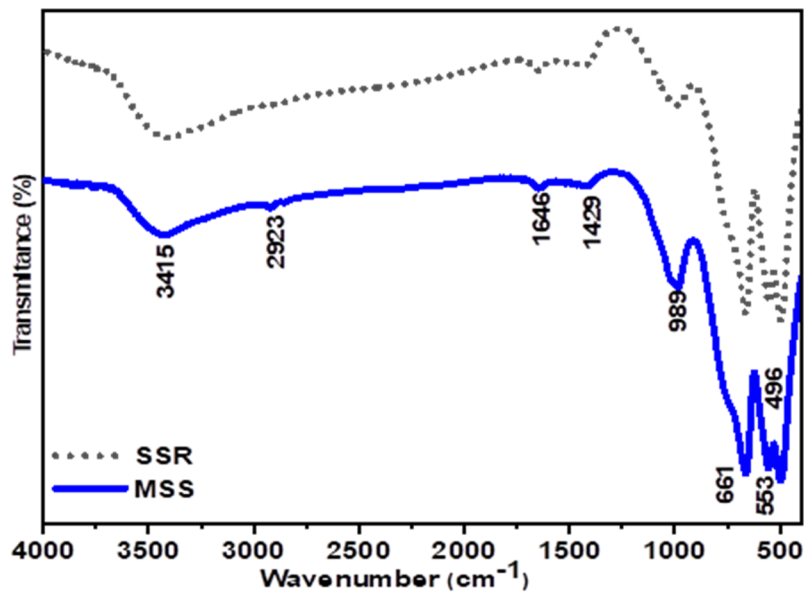


Fig. 5. FTIR spectra of zinc aluminate samples synthesized by both SSR and MSS.

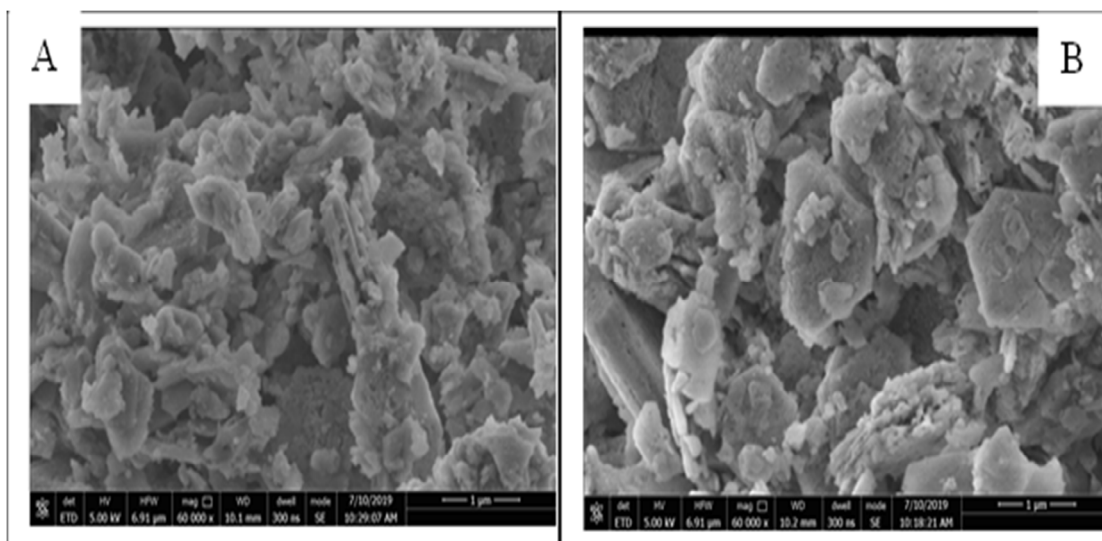


Fig. 6. SEM images of zinc aluminate samples synthesized by both SSR [A] and MSS [B].

and surface roughness. The small particles are dominant in the microstructure of the MSS sample, owing to the low degree of particle aggregation caused by the particles' covering by molten salt. This was responsible for the lower crystallinity of the MSS sample, which was seen in XRD analysis. According to the results of the SEM, the MSS sample has a higher structure homogeneity than the SSR sample, in which the product particles are formed from liquid phase reactants.

The microstructures of zinc aluminate samples synthesized by SSR (Fig. 7A, B) and MSS (Fig. 7C, D) were further investigated using high-resolution transmission electron microscopy (HRTEM). The formation of cubic zinc aluminate particles by both SSR and MSS was confirmed by TEM images, with particle sizes ranging from 5 to 100 nm. The microstructure of the SSR sample was characterized by particle aggregation and high crystallinity, and the cubic particles could be readily seen. For the MSS sample, the large plate-like particles were observed in image D, whereas, the high-resolution image C revealed the appearance of a huge number of very small particles. The average particle size concluded from the histograms is ~ 34 and 20 nm for both solid state and molten salt samples, respectively. This supports the SEM-based reaction mechanism for MSS, in which the particles form in two stages of a liquid-solid transition. The appearance of particles with a cubic structure for the SSR sample was revealed by selective area electron diffraction (SAED) (onset on image B), which confirms the

high crystallinity by the appearance of obvious light spots. Whereas for the MSS sample (onset on image D), the SAED image has a more pronounced cubic structure and light spots. Furthermore, the appearance of ordered light spots in six directions surrounding the cubic structure confirms the homogeneity of the MSS sample, in contrast to the appearance of a slightly confused and messy structure for the SSR sample. In addition to the high crystallinity of zinc aluminate samples synthesized by SSR and MSS, the superiority of the MSS sample over the SSR sample was also confirmed.

UV-visible absorption and photoluminescence emission spectroscopy were utilized to investigate the optical properties of MSS and SSR samples in terms of their absorbance efficiency and bandgap energy, as shown in Fig. 8A-C. Fig. 8A exhibits one absorption peak centered at 470 nm for both SSR and MSS samples, and a higher absorbance percent was observed for the MSS sample. The bandgap energy was estimated by constructing a Tauc plot relation between  $(\alpha h\nu)^2$  as a function of photon energy ( $h\nu$ ), where  $\alpha$  is the absorbance, as shown in Fig. 8B. It was found that the bandgap energy was reduced from 2.78 to 2.48 eV with the SSR modification by MSS.

The absorbance and bandgap energy of nanoscale materials are influenced by several factors, including crystallinity, particle size, surface roughness, and oxygen deficiency [10]. The presence of considerable numbers of OH-groups of surface adsorbed water molecules is the

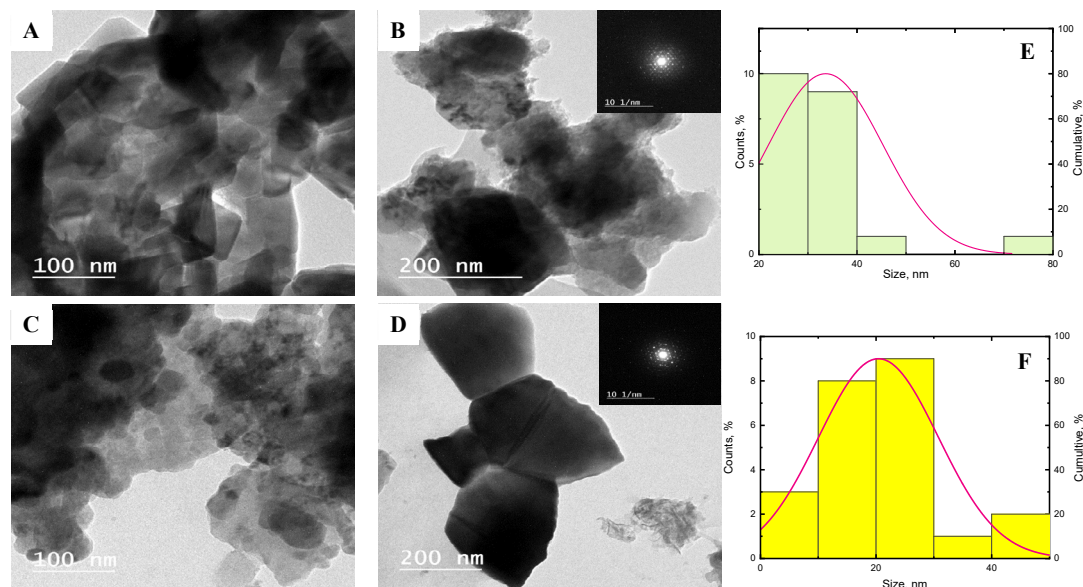


Fig. 7. TEM images of zinc aluminate samples synthesized by both SSR [A, B] and MSS [C, D], E & F are the histogram of both solid state and molten salt samples for particle size calculations, respectively.

fundamental explanation for the variation in the bandgap energy between SSR and MSS samples [30,31]. The discovery of Al-OH bond peaks at 989 and 1429  $\text{cm}^{-1}$  in the FTIR investigation, with higher intensity for the MSS sample, supports the presence of surface adsorbed water molecules. The MSS structure morphology was considerably changed by the Ostwald ripening processes, according to the scanning electron microscopy examination [28,29]. In which, the very small dissolved particles fall on the surface of the formally formed large particles, creating a rough surface. This roughness allows water molecules to enter surface pores and form oxygen vacancies, which causes a localized energy state in the zinc aluminate bandgap and lowers the bandgap energy compared to literature articles ( $\sim 3\text{-}3.9$  eV) [29,31–33].

Decreasing the bandgap energy could be linked to a phenomenon known as valence band orbital mixing, which has already been reported in the zinc aluminate structure. In which the zinc 3d orbital interferes with the oxygen 2p orbital, repulsing the valence band maximum up to the conduction band and lowering the bandgap energy to 2.78 eV [34].

Fig. 8C shows the photoluminescence spectroscopy of zinc aluminate samples synthesized by SSR and MSS samples. For both samples, a strong and intense peak centered at 470 nm, with higher intensity for the SSR sample. The bandgap value

determined by UV-visible spectroscopy matches well with the result acquired by photoluminescence spectroscopy. The difference in PL spectra intensities between the two samples was due to the difference in crystallinity and the presence of the OH-group of surface adsorbed water molecules [35]. The PL emission intensity increases as the OH content decreases; meanwhile, the low intensity of the PL peaks indicates a low electron-hole recombination rate, strong absorption, and high photocatalytic activity [36]. The optical properties of the zinc aluminate samples achieved by UV-visible and PL spectroscopy encouraged them to be used as photocatalytic materials for waste disposal, particularly in wastewater treatment.

#### Photocatalytic activity of zinc aluminate samples

Under visible light irradiation, the photocatalytic activities of zinc aluminate SSR and MSS samples in the photocatalytic degradation of brilliant cresyl blue dye (BCBD) were examined. The pH effect, the sample dose, and the dye concentration were all regulated in the photocatalytic degradation process. As shown in Fig. 9A-F, the effect of pH on the photocatalytic activity of SSR and MSS samples was examined by increasing the pH from 5 to 10 at a sample dose of 1 g/l and a dye concentration of 40 mg/l. Fig. 9A, B illustrate the change in relative concentration ( $C_t/C_0$ ) with time for both SSR and

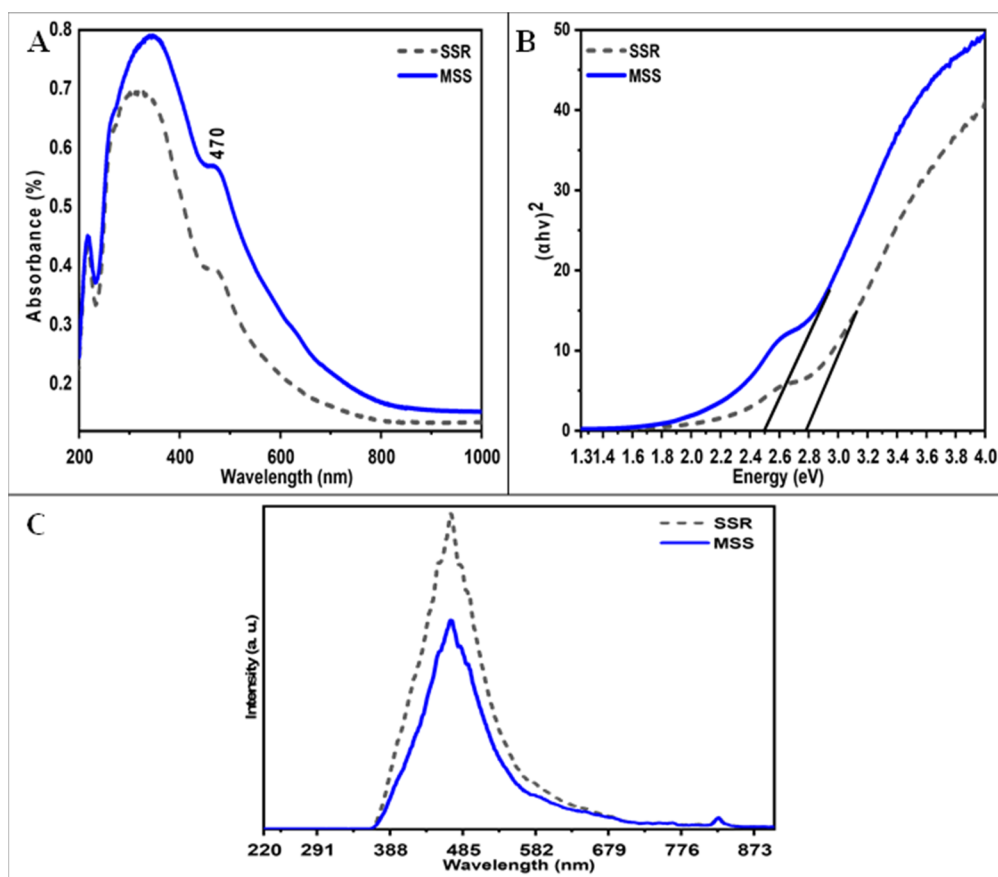


Fig. 8. UV-visible absorbance [A], the Tauc plot [B] and photoluminescence emission [C] curves of zinc aluminate samples synthesized by both SSR and MSS.

MSS samples, respectively, since  $C_0$  and  $C_t$  are the dye starting concentration and at time  $t$ . Samples proved high adsorption efficiency in the dark and high photocatalytic efficiency under visible light irradiation. The photocatalytic degradation percent of BCBD by MSS and SSR samples was plotted against time at different pH values of 5, 7, and 10, as shown in Figs. 9C and D, respectively. Degradation percent (D%) could be calculated using the following formula:  $D\% = [(C_0 - C_t)/C_0] * 100$

As shown in the Fig., the MSS sample has higher photocatalytic activity than the SSR sample. At pH 5, 7, and 10, the photocatalytic degradation of BCBD was 3.13, 10.6, and 18.61% in the dark, 20.57, 53.12, and 86.19% under visible light irradiation using the SSR sample, and 3.33, 11.8 and 22.5% in the dark, 32.35, 62.75 and 94.575% under visible light irradiation using the MSS sample, respectively. The pH parameter has a significant impact on photocatalytic degradation of BCBD; it increased

with increasing pH and reaches a maximum at pH 10 [37,38]. Figs. 9E and F show the absorption peak decay with increasing time duration for MSS and SSR samples, respectively, and prove that the concentration of BCBD decreases with increasing time duration.

The effect of sample dose on the photocatalytic degradation of BCBD was investigated by varying the MSS sample dose from 1- 0.25 g/l at constant pH 10 and a dye concentration of 40 mg/l, as shown in Fig. 10A. The sample dose had a significant impact on the photocatalytic degradation of BCBD, with the degradation percent decreasing from 94.575% to 65.15% and 52.5% when the sample dose was reduced from 1 g/l to 0.5 and 0.25 g/l, respectively. This result can be explained by the fact that decreasing the catalyst dose decreases the surface-active sites, and thus the electron-hole pair production, which is responsible for the production of the  $\text{OH}\cdot$  radical.

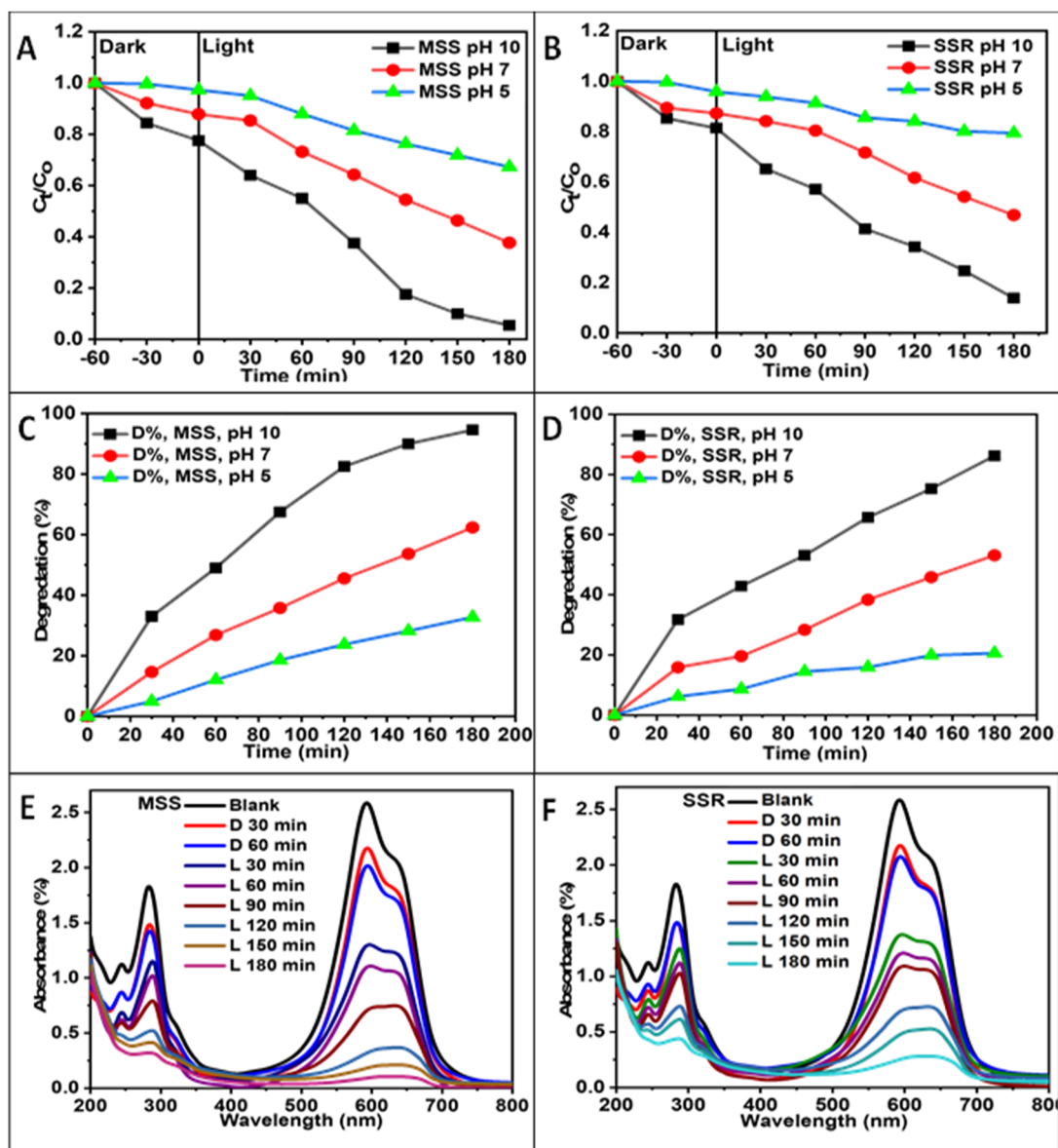


Fig. 9. the effect of pH on the photocatalytic activity of MSS and SSR samples; [A, B]: the change in relative dye concentration with time, [C, D]: degradation percent at different pH values, [E, F]: the absorption peak decay at pH 10, respectively.

As shown in Fig. 10B, the effect of dye concentration on the photocatalytic activity of the MSS sample was investigated by increasing the dye concentration from 40 mg/l to 80 mg/l at constant pH of 10 and a sample dose of 1 g/l. When the dye concentration was increased from 40 mg/l to 80 mg/l, the photocatalytic degradation percent of BCBD decreased from 94.575% to 65.9%. The inverse relationship between the degradation percent and the dye concentration was seen, as the dye particles completely cover the active

sites on the zinc aluminate surface and decrease its photocatalytic activity [39]. Furthermore, increasing the dye concentration reduces both the number of water molecules surrounding the zinc aluminate nanoparticles and the number of OH• radicals produced, both of which are required for photocatalytic degradation [40].

The reaction kinetics of BCBD photocatalytic degradation were investigated using MSS samples at various pH values with dye concentrations of 40 mg/l and sample doses of 1 g/l. Fig. 10C depicts a

Table 2. displays the kinetic data of BCBD photocatalytic degradation by using MSS sample, at various pH 5, 7 and 10.

Catalyst concentration	Sample dose	pH	$K$ ( $\text{min}^{-1}$ )	$r_0 \cdot 10^{-3}$ ( $\mu\text{M min}^{-1}$ )	$R^2$
40 mg/l	1 g/l	5	0.00222	15.8	0.99978
		7	0.00522	33	0.9988
		10	0.016	88.29	0.99817

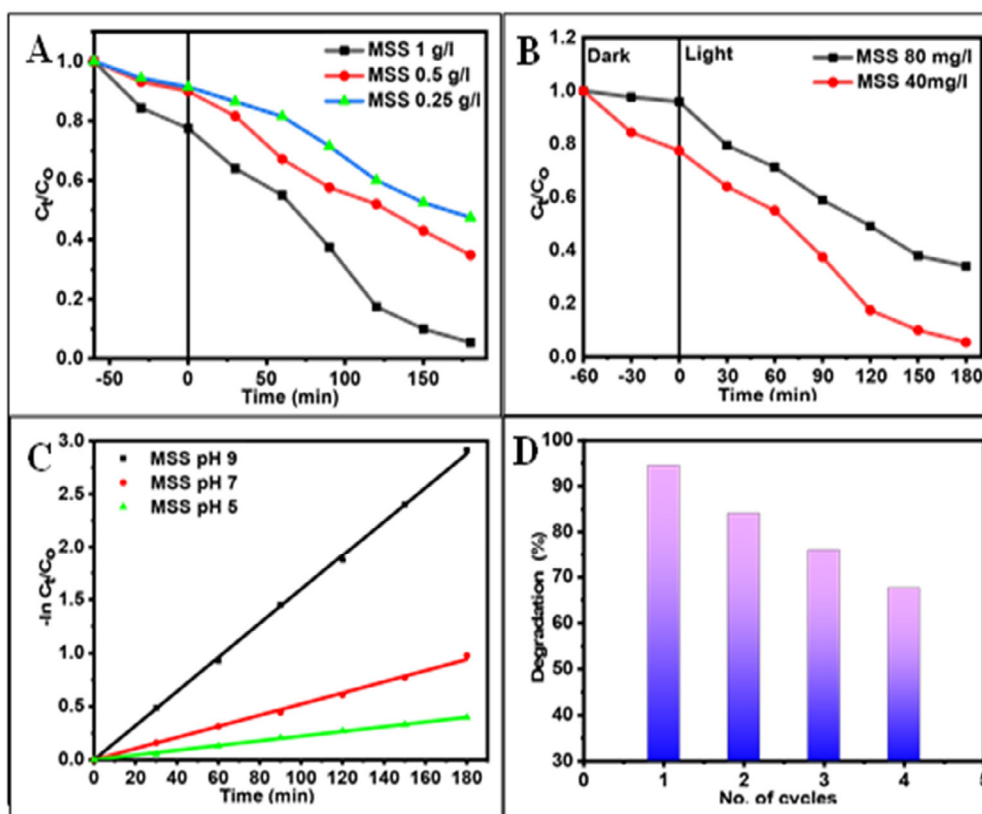


Fig. 10. the effect of sample dose [A], dye concentration [B], linear relation [C] and recyclable experiment [D] on the photocatalytic activity of MSS sample.

linear relationship ( $-\ln(C_t/C_0)$ ) plotted as a function of time. According to the formula:  $-\ln(C_t/C_0) = K t$

the photocatalytic degradation reaction is a first-order reaction, and the slope of this relationship equals the degradation rate constant ( $K$ ). At pH 5, 7, and 10, the values of  $K$  were 0.00222, 0.00522, and 0.016  $\text{min}^{-1}$ , respectively. The degradation rate ( $r_0$ ) was calculated by multiplying  $K$  ( $\text{min}^{-1}$ ) by the initial concentration of dye  $C_0$  ( $\mu\text{M}$ ), according to the formula:

$$r_0 = K C_0^n \quad \text{where } n \text{ is equal to unity for the first order reaction}$$

The fastest reaction rate was found to be  $88.29 \cdot 10^{-3} \mu\text{M min}^{-1}$  at pH 10. The obtained degradation rate is greater than that obtained by the authors ( $2.934 \cdot 10^{-7} \mu\text{M min}^{-1}$ ) for BCBD

degradation using another catalyst type [38]. The high reaction rate refers to the high photocatalytic activity of the synthesized zinc aluminate sample. The correlation coefficient ( $R^2$ ) was calculated after fitting the data on the origin pro program, and the values of all kinetic parameters are listed in Table 2.

The recyclable experiment was repeated several times to evaluate the photocatalytic stability of the zinc aluminate MSS sample in the photocatalytic degradation of BCBD. Fig. 10D depicts four runs of photocatalytic degradation at the collected optimum conditions, yielding 94.575, 84.127, 75.98, and 67.58% degradation in the first, second, third, and fourth runs, respectively. Although photocatalytic degradation was reduced with recycling, MSS zinc aluminate achieved high

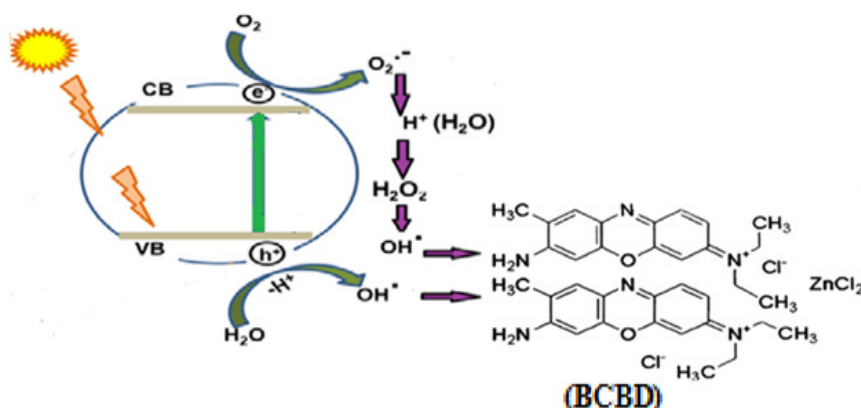
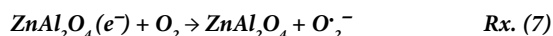
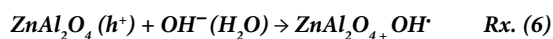
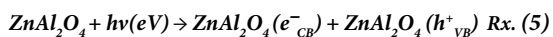


Fig. 11. the schematic view of the BCBD degradation mechanism by using zinc aluminate MSS sample as a photocatalyst.

photocatalytic efficiency in the fourth run. This demonstrated that the synthesized zinc aluminate MSS sample is stable as a photocatalytic material when exposed to visible light.

The reaction mechanism of BCBD photocatalytic degradation using zinc aluminate as a photocatalyst was discussed as the following: Since BCBD is a cationic dye, the degradation reaction was enhanced in an alkaline medium by the action of the  $\text{OH}^\cdot$  radical [38]. The high pH value enhances the formation of negatively charged particles and supports the formation of  $\text{OH}^\cdot$  radicals [41]. Radiation of zinc aluminate by visible light results in excitation of the valence band electron to the conduction band leaving a hole ( $\text{h}^+$ ) in the valence band, according to reaction (5). These electron-hole pairs help in the photocatalytic degradation of BCBD, in which, the hole can be trapped by the hydroxyl group of the surrounding water, forming an  $\text{OH}^\cdot$  radical, according to reaction (6). According to reaction (7), electrons can be trapped from the conduction band by the superoxide anion, forming a superoxide anion radical ( $\text{O}_2^{\cdot-}$ ). This radical ( $\text{O}_2^{\cdot-}$ ) indirectly influences the photocatalytic degradation of BCBD since it reacts with water, forming hydrogen peroxide, which by role is transferred to the  $\text{OH}^\cdot$  radical, according to reaction (8). The produced  $\text{OH}^\cdot$  radical attacks the BCBD, transforming it into oxidized products (organic ashes), according to reaction (9). The photocatalytic degradation mechanism was illustrated from a schematic point of view in Fig. 11.



The change in MSS sample structure was studied by XRD analysis after performing the recyclable experiment, as shown in Fig. 12. Sample crystallinity was reduced after the fourth run with the appearance of an amorphous structure at  $2\theta \sim 20\text{-}30^\circ$ , including two impurity peaks certainly located at  $2\theta = 20.3^\circ$  and  $30.14^\circ$ .

Following the degradation process, the dye solution was subjected to TOC analysis under optimum conditions of pH, dye concentration, and sample dose. The photocatalytic degradation percent was calculated as  $D\% = (\text{TOC}_0 - \text{TOC}_t) / \text{TOC}_0 * 100$ , where  $\text{TOC}_0$  and  $\text{TOC}_t$  are the total organic carbon at the end of the darkness test and the light exposure, respectively. In comparison to the UV-visible spectroscopy result (94.575%), the TOC results revealed that approximately 67.5% of the BCBD was degraded, implying the formation of uncolored by-products.

Some recent studies on photocatalytic degradation of the complex structure BCBD will be discussed. The BCBD is widely used in the textile industry, but it is environmentally hazardous and resistant to degradation. Under visible light irradiation, the degradation percent was maximized at 80% in a long time duration reaching 8 h, using a high catalyst dose of 3.5 g/L of  $\text{TiO}_2$  [42]. Under

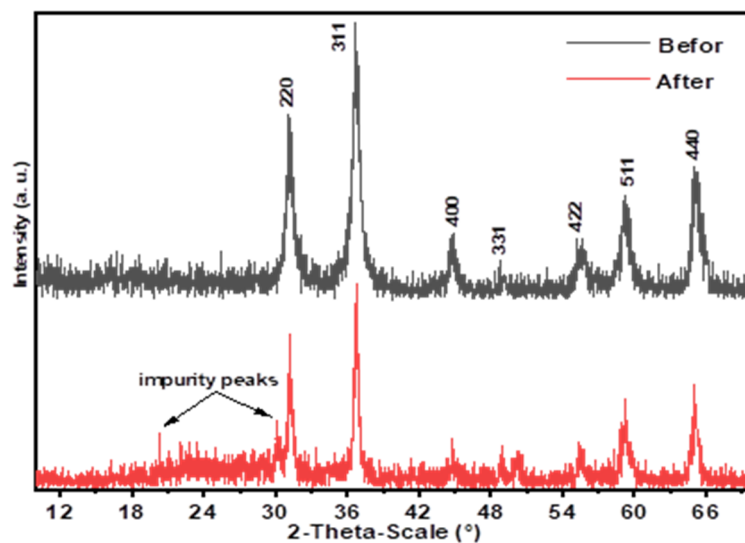


Fig. 12. XRD patterns of MSS sample before and after applying the recyclable experiment.

Table 3. summarizes the published literature articles on the photocatalytic degradation of brilliant cresyl blue dye (BCBD).

Reference	Light source	Catalyst type	Catalyst dose (g/L)	Dye conc. (mg/L)	Duration time (h)	Degradation % (max.)
Swami, Pare, and Pandit [42]	Visible light	TiO <sub>2</sub>	0.5-3.5	4-20	8 h	80
S. B. Khan et al. [37]	Sun light	ZnMn <sub>2</sub> O <sub>4</sub>	1.132-1.193	40	2 h	83
Hazim Y. Al-Gubury and Al – Murshidy [43]	UV light	ZnO	0.2-5	3-30	1 h	98
Asif, Khan, and Asiri [38]	Sun light	Al <sub>2</sub> O <sub>3</sub> doped Mn <sub>3</sub> O <sub>4</sub>	1.132-1.193	40	5 h	65
Hazim Yahya Al-Gubury et al. [40]	Sun light	Al <sub>2</sub> O <sub>3</sub>	0.7-4.5	50-90	1 h	92.8
This study	Visible light	ZnAl <sub>2</sub> O <sub>4</sub>	1	40-80	3 h	94.5

UV-light irradiation, degradation percent was found to be maximized at 98% using 5 g/l of ZnO [43]. The degradation process was employed with a high catalyst dose while using UV-light irradiation. Furthermore, BCBD was degraded in the literature by sunlight irradiation, with the degradation percent reaching 65, 90, and 92.87% using a high catalyst dose of Al<sub>2</sub>O<sub>3</sub>/Mn<sub>3</sub>O<sub>4</sub>, ZnMn<sub>2</sub>O<sub>4</sub>, and Al<sub>2</sub>O<sub>3</sub> (1.193 g/L and 4.5 g/l), respectively [37,38,40]. In this study, 94.5% of the dye was degraded by using 1 g/L of ZnAl<sub>2</sub>O<sub>4</sub> under visible light irradiation. Table 3 contains a list of articles on the photocatalytic degradation of BCBD.

Furthermore, the photocatalytic activity of the synthesized zinc aluminate in the degradation

of various organic dyes is compared with the literature. Zinc aluminate was previously used for photocatalytic degradation of dyes as like as, reactive red 141 and direct black 38 under sunlight irradiation, degradation percent reached 100 and 99% in long time duration of 5 and 4 h, respectively [4,44]. Whereas, under UV-light, zinc aluminate achieved 100, 90 and 20% for low concentration 10 mg/l of rhodamine b, methylene blue and crystal violet [10,45,46], respectively. While using of UV-light, a low concentration of dye was used. On the other side, high activity is proved in this study under visible light irradiation for a high concentration (40 mg/l) of complex structure brilliant cresyl blue dye. These results were summarized in Table 4.

Table 4. summarizes the published literature articles on the photocatalytic degradation of various organic dyes using zinc aluminate as photocatalyst.

Reference	Light source	Catalyst dose (g/l)	Type of dye	Dye conc. (mg/L)	Duration time (h)	Degradation % (max.)
Foletto et al. [44]	Sun light	1	Reactive red 141	70 mg/l	5	100 %
Zhao, Li, and Zhao [46]	UV light	1	Rhodamine B	20 mg/l	1	100 %
Ragul and Sumathi [45]	UV light	1	Rhodamine B and crystal violet	10 mg/l	2	20 %
Battiston et al. [4]	Sun light	1	Direct black 38	80-200 mg/l	4	30-99 %
Rahman, Charoo, and Jayaganthan [10]	UV light	0.1	Methylene blue	10 mg/l	5	90 %

## CONCLUSION

Solid industrial wastes such as aluminum and zinc sludges were used to synthesize nanosized zinc aluminate powder. XRD, XRF, and DTA investigations were used to characterize aluminum and zinc sludges. The findings revealed that aluminum and zinc were detected in their sludges as gibbsite minerals ( $\text{Al}(\text{OH})_3$ ) and hydrozincite ( $\text{Zn}_5(\text{CO}_3)_2(\text{OH})_6$ ), respectively. The thermal stability of the sludge mixture at temperatures exceeding  $730^\circ\text{C}$  was confirmed by thermal analysis. By using potassium chloride (KCl) as a molten salt, solid-state reaction (SSR) and molten salt synthesis (MSS) were carried out at the same temperature of  $1100^\circ\text{C}$ . XRD, FTIR, and XPS analyses were used to assess the structural properties of the synthesized samples, and the results revealed that pure phase zinc aluminate nanoparticles were synthesized. The SEM investigation was used to examine the structural morphology of the synthesized samples, and the microstructure of the MSS sample was found to be more homogeneous than that of the SSR sample. For both SSR and MSS routs, the high-resolution TEM supports the SEM result and expresses more details linked to particle growth according to a particular mechanism. In terms of absorbance efficiency and bandgap energy, SSR and MSS samples were studied using UV-visible and PL spectroscopy. Samples demonstrated excellent optical properties, promoting them for photocatalytic applications such as dye removal from wastewater. SSR and MSS samples were utilized in the photocatalytic degradation of the brilliant cresyl blue dye (BCBD). In addition to its high photocatalytic stability under visible light irradiation, the MSS sample proved high photocatalytic activity with a 94.5% degradation at the optimum conditions of pH, sample dose, and dye concentration.

## CONFLICT OF INTEREST

The authors declare that there are no conflicts of interest regarding the publication of this paper.

## REFERENCES

- [1] V.S. Pinto, A.P. Luz, O.H. Borges, V.C. Pandolfelli, Binder effect on  $\text{ZnAl}_2\text{O}_4$ -containing high-alumina refractory castables, *Ceram. Int.* 48 (2022) 11401-11409. <https://doi.org/10.1016/j.ceramint.2021.12.363>
- [2] M. Shaban, R. Hosny, A.M. Rabie, J.J. Shim, S.A. Ahmed, M.A. Betiha, N.A. Negm, Zinc aluminate nanoparticles: Preparation, characterization and application as efficient and economic catalyst in transformation of waste cooking oil into biodiesel, *J. Mol. Liq.* 302 (2020) 112377. <https://doi.org/10.1016/j.molliq.2019.112377>
- [3] P. Pipattanaporn, P. Pansiri, P. Kumpeerakij, S. Yaemphuchong, P. Siri-apai, N. Suetrong, K. Chansaenpak, S. Singkammo, P. Kanjanaboos, Y. Hanlumyuang, S. Wannapaiboon, W. Wattanathana, Effect of triethanolamine chelating agent on crystallinities, phase purities, and optical properties of zinc aluminate spinel synthesized by thermal decomposition, *Ceram. Int.* 48 (2022) 8186-8195. <https://doi.org/10.1016/j.ceramint.2021.12.021>
- [4] S. Battiston, C. Rigo, E. Da Cruz Severo, M.A. Mazutti, R.C. Kuhn, A. Gündel, E.L. Foletto, Synthesis of zinc aluminate ( $\text{ZnAl}_2\text{O}_4$ ) Spinel and its application as photocatalyst, *Mater. Res.* 17 (2014) 734-738. <https://doi.org/10.1590/S1516-14392014005000073>
- [5] S. Siragam, R.S. Dubey, L. Pappula, G. Sathesh Babu, Synthesis and investigation of dielectric ceramic nanoparticles for microstrip patch antenna applications, *Sci. Rep.* 12 (2022) 1-10. <https://doi.org/10.1038/s41598-022-07899-6>
- [6] R. Venkatesh, L.S.R. Yadav, N. Dhananjaya, Rare earth activated bio synthesis of zinc aluminate for photocatalytic activity of dye, *Mater. Today Proc.* 49 (2021) 628-631. <https://doi.org/10.1016/j.matpr.2021.04.534>
- [7] V. Baiju, D. Devadathan, G. Sajeekumar, Photocatalytic degradation of toxic organic pollutants using zinc aluminate nanocomposite, *Mater. Today Proc.* 47 (2021) 1507-1513. <https://doi.org/10.1016/j.matpr.2021.06.066>
- [8] A.T.S.P. Putra, An improved method for high photocatalytic performance of  $\text{ZnAl}_2\text{O}_4$  spinel derived from layered double hydroxide precursor, *SN Appl. Sci.* 2 (2020) 1-10. <https://doi.org/10.1007/s42452-020-2682-7>
- [9] L.E. Sotelo Martin, R.H.R. Castro, Al excess

- extends Hall-Petch relation in nanocrystalline zinc aluminate, *J. Am. Ceram. Soc.* 105 (2022) 1417-1427. <https://doi.org/10.1111/jace.18176>
- [10] A. Rahman, M.S. Charoo, R. Jayaganthan, Structural, optical and photocatalytic properties of zinc aluminate spinel nanoparticles, *Mater. Technol.* 30 (2015) 168-176. <https://doi.org/10.1179/1753555714Y.0000000211>
- [11] V. Baiju, D. Devadathan, P. Rejani, G. Sajeekumar, R. Raveendran, Effect of annealing temperature in the purity of zinc aluminate synthesized by solution combustion method, *AIP Conf. Proc.* 2379 (2021). <https://doi.org/10.1063/5.0058365>
- [12] S. Siragam, R.S. Dubey, L. Pappula, Investigation of structural, chemical, morphological and dielectric properties of sol-gel derived ZnAl<sub>2</sub>O<sub>4</sub> nanoparticles, *Mater. Today Proc.* 45 (2021) 2091-2095. <https://doi.org/10.1016/j.matpr.2020.09.629>
- [13] X. Wei, D. Chen, Synthesis and characterization of nanosized zinc aluminate spinel by sol-gel technique, *Mater. Lett.* 60 (2006) 823-827. <https://doi.org/10.1016/j.matlet.2005.10.024>
- [14] Z. Li, S. Zhang, W.E. Lee, Molten salt synthesis of zinc aluminate powder, *J. Eur. Ceram. Soc.* 27 (2007) 3407-3412. <https://doi.org/10.1016/j.jeurceramsoc.2007.02.195>
- [15] C. Sikalidis, *Advances in Ceramics - Synthesis and Characterization, Processing and Specific Applications*, 2012. <https://doi.org/10.5772/985>
- [16] J. Vereš, Š. Jakabský, M. Lovás, Zinc recovery from iron and steel making wastes by conventional and microwave assisted leaching, *Acta Montan. Slovaca.* 16 (2011) 185-191.
- [17] A.I. Arogundade, F. Ahmad, A.H. Bhat, Q.F. Gillani, P.S.M.B. Megat-Yusoff, Investigating the Synergistic Effect of BauxsolTM in an Epoxy Intumescent Coating System, *Procedia Eng.* 148 (2016) 223-227. <https://doi.org/10.1016/j.proeng.2016.06.579>
- [18] M. Carbone, R. Briancesco, L. Bonadonna, Antimicrobial power of Cu/Zn mixed oxide nanoparticles to *Escherichia coli*, *Environ. Nanotechnology, Monit. Manag.* 7 (2017) 97-102. <https://doi.org/10.1016/j.enmm.2017.01.005>
- [19] Q.W. Zhan, C.X. Qian, Microbial-induced synthesis of nanoparticles of zinc phosphate and basic zinc carbonate based on the degradation of glyphosate, *Dig. J. Nanomater. Biostructures.* 11 (2016) 393-399.
- [20] N. Kanari, D. Mishra, I. Gaballah, B. Dupré, N. Kanari, D. Mishra, I. Gaballah, B. Dupré, Thermal decomposition of zinc carbonate hydroxide., *Thermochim. Acta, Elsevier.* 410 (2004) 93-100. [https://doi.org/10.1016/S0040-6031\(03\)00396-4](https://doi.org/10.1016/S0040-6031(03)00396-4)
- [21] I.U. Haq, A.M. Azad, Experimental artifacts for morphological tweaking of chemical sensor materials: Studies on ZnO, *Sensors (Switzerland).* 12 (2012) 8259-8277. <https://doi.org/10.3390/s120608259>
- [22] C.M. Earnest, K.G. and Britney, Stong, Improved Quantification of Gibbsite in Bauxite Ores by Thermogravimetric Methods (TGA and DTG), *Adv. Appl. Chem. Biochem.* 1 (2018) 9-17. <https://doi.org/10.33513/ACBC/1801-02>
- [23] J.T. Klopogge, H.D. Ruan, R.L. Frost, Thermal decomposition of bauxite minerals: Infrared emission spectroscopy of gibbsite, boehmite and diaspor, *J. Mater. Sci.* 37 (2002) 1121-1129. <https://doi.org/10.1023/A:1014303119055>
- [24] S. Abd El All, Y.H.A. Fawzy, R.M. Radwan, Study on the structure and electrical behaviour of zinc aluminate ceramics irradiated with gamma radiation, *J. Phys. D. Appl. Phys.* 40 (2007) 5707-5713. <https://doi.org/10.1088/0022-3727/40/18/029>
- [25] B.R. Strohmeyer, Zinc Aluminate (ZnAl<sub>2</sub>O<sub>4</sub>) by XPS, *Surf. Sci. Spectra.* 3 (1994) 128-134. <https://doi.org/10.1116/1.1247773>
- [26] S. Sunder, S. Rohilla, S. Kumar, P. Aghamkar, Structural characterization of spinel zinc aluminate nanoparticles prepared by coprecipitation method, *AIP Conf. Proc.* 1393 (2011) 123-124. <https://doi.org/10.1063/1.3653640>
- [27] K. Nagata, K. Sato, K.S. Goto, Kinetics of the solid state reaction between zinc oxide and aluminum oxide, *Metall. Trans. B.* 11 (1980) 455-461. <https://doi.org/10.1007/BF02676889>
- [28] Mohamed N. Rahaman, *Ceramic processing and sintering*, 1996.
- [29] X.Y. Chen, C. Ma, Z.J. Zhang, B.N. Wang, Ultrafine gahnite (ZnAl<sub>2</sub>O<sub>4</sub>) nanocrystals: Hydrothermal synthesis and photoluminescent properties, *Mater. Sci. Eng. B Solid-State Mater. Adv. Technol.* 151 (2008) 224-230. <https://doi.org/10.1016/j.mseb.2008.09.023>
- [30] M.M. Khan, S.A. Ansari, D. Pradhan, D.H. Han, J. Lee, M.H. Cho, Defect-induced band gap narrowed CeO<sub>2</sub> nanostructures for visible light activities, *Ind. Eng. Chem. Res.* 53 (2014) 9754-9763. <https://doi.org/10.1021/ie500986n>
- [31] S. Sumathi, A. Kavipriya, Structural, optical and photocatalytic activity of cerium doped zinc aluminate, *Solid State Sci.* 65 (2017) 52-60. <https://doi.org/10.1016/j.solidstatesciences.2017.01.003>
- [32] S.F. Wang, G.Z. Sun, L.M. Fang, L. Lei, X. Xiang, X.T. Zu, A comparative study of ZnAl<sub>2</sub>O<sub>4</sub> nanoparticles synthesized from different aluminum salts for use as fluorescence materials, *Sci. Rep.* 5 (2015) 1-12. <https://doi.org/10.1038/srep12849>
- [33] S. Mathur, M. Veith, M. Haas, H. Shen, N. Leccerf, V. Huch, S. Hüfner, R. Haberkorn, H.P. Beck, M. Jilavi, Single-Source Sol-Gel Synthesis of Nanocrystalline ZnAl<sub>2</sub>O<sub>4</sub>: Structural and Optical Properties, *J. Am. Ceram. Soc.* 84 (2004) 1921-1928. <https://doi.org/10.1111/j.1151-2916.2001.tb00938.x>
- [34] S.K. Sampath, D.G. Kanhere, R. Pandey, Electronic structure of spinel oxides: Zinc aluminate and zinc gallate, *J. Phys. Condens. Matter.* 11 (1999) 3635-3644. <https://doi.org/10.1088/0953-8984/11/18/301>
- [35] M.T. Tsai, Y.S. Chang, I.B. Huang, B.Y. Pan, Luminescent and structural properties of manganese-doped zinc aluminate spinel nanocrystals, *Ceram. Int.* 39 (2013) 3691-3697. <https://doi.org/10.1016/j.ceramint.2012.10.201>
- [36] S.F. Yang, C.G. Niu, D.W. Huang, H. Zhang, C. Liang, G.M. Zeng, SrTiO<sub>3</sub> nanocubes decorated with Ag/AgCl nanoparticles as photocatalysts with enhanced visible-light photocatalytic activity towards the degradation of dyes, phenol and bisphenol A, *Environ. Sci. Nano.* 4 (2017) 585-595. <https://doi.org/10.1039/C6EN00597G>
- [37] S.B. Khan, M.M. Rahman, K. Akhtar, A.M. Asiri, Nitrophenol Chemi-Sensor and Active Solar Photocatalyst Based on Spinel Nitrophenol Chemi-Sensor and Active Solar Photocatalyst Based on Spinel Hetaerolite Nanoparticles, *PLoS One.* 9 (2014) 1-8. <https://doi.org/10.1371/journal.pone.0085290>
- [38] S.A. Bin Asif, S.B. Khan, A.M. Asiri, Visible light functioning photocatalyst based on Al<sub>2</sub>O<sub>3</sub> doped

- Mn<sub>3</sub>O<sub>4</sub> nanomaterial for the degradation of organic toxin, *Nanoscale Res. Lett.* 10 (2015) 1-10. <https://doi.org/10.1186/s11671-015-0990-4>
- [39] S.I. El-Hout, S.M. El-Sheikh, A. Gaber, A. Shawky, A.I. Ahmed, Highly efficient sunlight-driven photocatalytic degradation of malachite green dye over reduced graphene oxide-supported CuS nanoparticles, *J. Alloys Compd.* 849 (2020) 156573. <https://doi.org/10.1016/j.jallcom.2020.156573>
- [40] H.Y. Al-Gubury, H.S. Alteemi, A.M. Saad, R.R. Al-Shamary, Removal of hazardous brilliant cresyl blue dye utilizing aluminum oxide as photocatalyst, *Indones. J. Chem.* 19 (2019) 292-297. <https://doi.org/10.22146/ijc.30135>
- [41] G. Zhang, M.N. Nadagouda, K. O'Shea, S.M. El-Sheikh, A.A. Ismail, V. Likodimos, P. Falaras, D.D. Dionysiou, Degradation of cylindrospermopsin by using polymorphic titanium dioxide under UV-Vis irradiation, *Catal. Today.* 224 (2014) 49-55. <https://doi.org/10.1016/j.cattod.2013.10.072>
- [42] D. Swami, B. Pare, P. Pandit, Decolorization and mineralization of hazardous brilliant cresyl blue dye using visible light and TiO<sub>2</sub> as photocatalyst, *Nat. Environ. Pollut. Technol.* 15 (2016) 123-128.
- [43] H.Y. Al-Gubury, G.S. Al - Murshidy, Photocatalytic decolorization of brilliant cresyl blue using zinc oxide, *Int. J. PharmTech Res.* 8 (2015) 289-297.
- [44] E.L. Foletto, S. Battiston, J.M. Simões, M.M. Bassaco, L.S.F. Pereira, É.M. De Moraes Flores, E.I. Müller, Synthesis of ZnAl<sub>2</sub>O<sub>4</sub> nanoparticles by different routes and the effect of its pore size on the photocatalytic process, *Microporous Mesoporous Mater.* 163 (2012) 29-33. <https://doi.org/10.1016/j.micromeso.2012.06.039>
- [45] G. Ragul, S. Sumathi, Synthesis, characterization and photocatalytic study of zinc aluminate nanopowders against Rhodamine-B and crystal violet dyes, *Int. J. Appl. Eng. Res.* 8 (2013) 2175-2178.
- [46] L. Zhao, X. Li, J. Zhao, Fabrication, characterization and photocatalytic capability of ZnAl<sub>2</sub>O<sub>4</sub> nanospheres, *Adv. Mater. Res.* 518-523 (2012) 736-739. <https://doi.org/10.4028/www.scientific.net/AMR.518-523.736>